



Complex Epitaxy of Tetragonal Tungsten Bronze K-Ta-Nb-O Nanorods

Valérie Demange, Quentin Simon, F. Gouttefangeas, Loïc Joanny, Maryline
Guilloux-Viry

► To cite this version:

Valérie Demange, Quentin Simon, F. Gouttefangeas, Loïc Joanny, Maryline Guilloux-Viry. Complex Epitaxy of Tetragonal Tungsten Bronze K-Ta-Nb-O Nanorods. *Crystal Growth & Design*, 2020, 20 (4), pp.2356-2366. 10.1021/acs.cgd.9b01501 . hal-02797038

HAL Id: hal-02797038

<https://univ-rennes.hal.science/hal-02797038>

Submitted on 15 Jun 2020

HAL is a multi-disciplinary open access archive for the deposit and dissemination of scientific research documents, whether they are published or not. The documents may come from teaching and research institutions in France or abroad, or from public or private research centers.

L'archive ouverte pluridisciplinaire **HAL**, est destinée au dépôt et à la diffusion de documents scientifiques de niveau recherche, publiés ou non, émanant des établissements d'enseignement et de recherche français ou étrangers, des laboratoires publics ou privés.

Complex epitaxy of tetragonal tungsten bronze K-Ta-Nb-O nanorods

V. Demange^{1,2}, Q. Simon³, F. Gouttefangeas², L. Joanny², M. Guilloux-Viry^{1,2}*

¹Univ Rennes, CNRS, ISCR –UMR 6226, F-35000 Rennes, France

²Univ Rennes, CNRS, ScanMAT–UMS 2001, F-35000 Rennes, France

³GREMAN, UMR 7347 CNRS - Université de Tours, F-37200 Tours, France

KEYWORDS. KTN; TTB; thin films;

ABSTRACT. Tetragonal tungsten bronze phases possess numerous important properties (ferroelectricity, multiferroicity, piezoelectricity, optical non-linearity, electro-optics) that can be achieved by modifying their composition, in addition to their ability to grow as very anisotropic crystals. In this study, $K_{5.06}(Ta_{0.57}Nb_{0.43})_{10.99}O_{30}$ tetragonal tungsten bronze phase thin films have been grown by pulsed laser deposition technique on (001)SrTiO₃

and R-plane sapphire substrates. The films have grown according to two modes with respect to the substrate surface, *i.e.* as vertical nanorods with the [001] direction perpendicular to the substrate surface, and as horizontal nanorods with the [001] orientation parallel to the substrate surface and $\langle 310 \rangle$ out-of-plane direction. Both vertical and horizontal nanorods present epitaxial relationships with the substrates. Careful study of epitaxial relationships showed a complex growth on both substrates that can be described in the framework of domain matching epitaxy resulting in several anti-phase domains formation for both kind of nanorods. These particular configurations are due to a high degree of coincidence between cations (anions) of the film with those of the substrate. This study shows the ability of ferroelectric TTB phases to grow as one-dimensional objects with the possibility to tailor their polarization direction either normal to or parallel to the substrate surface.

1. INTRODUCTION

Piezoelectric materials produce an electrical signal in response to an applied force. Such materials are intensively used in numerous fields of the modern society (*e.g.* actuators, sensors, transducers for information, communications, industrial automation, medical diagnostics, energy

harvesters from vibrations, *etc.*). Most devices use polycrystalline ceramics, in particular lead zirconate titanate $\text{PbZr}_{1-x}\text{Ti}_x\text{O}_3$ (PZT) oxides that are up-to-date the most performant piezoelectric materials¹. However, PZT materials contain a large amount of lead which is highly toxic. Governmental directives in Europe against hazardous substances have restricted the use of lead-based materials and oriented the research toward the exclusion or substitution of lead in electronic devices^{2,3}. Efforts on new lead-free materials have been mainly devoted to phases crystallizing in the perovskite structure, like BaTiO_3 ⁴ and $(\text{K},\text{Na})\text{NbO}_3$ (KNN)^{1,5}. Even though they do not have the highest piezoelectric properties, lead-free materials can show a better efficiency with limitations of losses in the transfer of energy. State of the art materials may become competitive with lead-based materials but for limited devices and applications⁶. Therefore, research on new lead-free materials is still needed.

Beyond the intrinsic properties of a given composition, the shape of the piezoelectric material is also subject to intensive research with the development in recent past years of integrated piezoelectric nanogenerators, that are either based on piezoelectric thin films or on one dimensional (1D) nanostructures^{1,7}. However, the piezoelectric performances of films or nanostructures are lower compared with that of single crystals. In most cases, lead-based and lead-free 1D nanostructures exhibit a polycrystalline and highly defective microstructure, that is deleterious for their intrinsic properties⁸. Therefore, a synthesis method of piezoelectric single-crystalline nanostructures with controlled orientation (thus polarization direction), with very few process steps, is of great interest.

In this context, the tetragonal tungsten bronze (TTB) phases, that received little attention up to now compared to perovskite phases, are subject to increasing researches in reason of their numerous important properties (ferroelectricity, multiferroicity, piezoelectricity, optical non-

linearity, electro-optics^{9–11}) that can be achieved by modifying their composition, in addition to their ability to grow as very anisotropic crystals^{12–14}. The crystallographic cell of most of the lead-free TTB niobates is strongly anisotropic (figure 1a,b) with $a_{\text{TTB}} \sim 12.5 \text{ \AA}$, and $c_{\text{TTB}} \sim 4 \text{ \AA}$ (space group (SG): $P4/mbm$ (paraelectric phase) or $P4bm$ (ferroelectric phase with the polarization direction along the $[001]$ direction)¹⁵.

Their chemical formula is $A_1A_2A_4C_4B_1B_2O_{30}$ where A1, A2, B1, B2 and C (figure 1c) are crystallographic sites partially or fully occupied by cations located in squared (A1), pentagonal (A2) and triangular (C) tunnels formed by B_1O_6 and B_2O_6 distorted octahedra which are connected by apices. A1 and A2 sites are generally occupied by alkaline (K^+ , Na^+ , ...) and alkaline earth (Ca^{2+} , Sr^{2+} , Ba^{2+} , ...) cations, whereas B1 and B2 sites are occupied by small and highly charged cations as Nb^{5+} , which can be partially substituted by transition metals cations of different valences¹⁰. In most TTB compounds, the C sites are empty, but can be occupied by small cations¹⁶. When all the A1/A2 sites are fully occupied ("filled TTB"), the TTB crystals synthesized by solid state reaction methods usually grow as rods, the crystallographic anisotropy inducing a microstructural anisotropy. These rods can be as long as few millimetres, depending on the elements located in A1 and A2 sites^{12–14}. In a previous work, we reported the growth of about 1 μm long $K_{5.06}(Ta_{0.57}Nb_{0.43})_{10.99}O_{30}$ (KTN) TTB parallelepiped-shaped nanorods ($a_{\text{TTB}} = 12.537 \text{ \AA} \pm 0.003 \text{ \AA}$, $c_{\text{TTB}} = 3.975 \text{ \AA} \pm 0.001 \text{ \AA}$) on $(\bar{1}102)$ Al_2O_3 (R-plane sapphire) by pulsed laser deposition¹⁷. This niobate grows according to 2 modes with respect to the substrate surface: (i) as vertical nanorods with the $[001]$ direction parallel to the surface substrate normal, and (ii) as horizontal nanorods with the $[001]$ parallel to the substrate surface, as schematized in figure 2a.

As the physical properties of ferroelectric film depend on the polarization direction, therefore on the preferential orientation, it is mandatory to know the growth behaviour on

single crystalline substrates. On the basis of this previous work, we studied here the structural growth relationships of KTN-TTB films on R-plane sapphire and on (001) SrTiO_3 (STO) single crystal substrates, and showed that the films exhibit epitaxial relationships with both substrates. These two substrates are of great interest. Indeed, in spite of the difference of the structure of these two substrates, both can promote the epitaxial growth of TTB oxides, possibly with different state of strains. In addition, whereas SrTiO_3 is a model substrate for the growth of many oxide thin films and suitable for many applications, in particular at low frequency, like piezoelectricity, sapphire is available in large dimensions and suitable for a large variety of applications including high frequency range thanks to its low dielectric permittivity and low dielectric losses. We describe the epitaxy relationships and discuss the results in relation with energetically preferential configurations.

2. EXPERIMENTAL SECTION

The pulsed laser deposition (PLD) target, of composition $\text{KTa}_{0.65}\text{Nb}_{0.35}\text{O}_3 + 60 \text{ mol. } \%$ KNO_3 , was prepared by sintering a mixture of KNbO_3 , KTaO_3 and KNO_3 powders at 350°C

for 12 h (KNO_3 was used in order to introduce a potassium excess to counterbalance the depletion of potassium stoichiometry occurring during the deposition, due to the high volatility of potassium oxide K_2O under high temperature)¹⁸. KNbO_3 (KTaO_3) compound was prepared by solid state reaction from Nb_2O_5 (Ta_2O_5) and $\text{K}_2\text{CO}_3 \cdot 1.5\text{H}_2\text{O}$ precursors at 1000°C for 12 h. The KNO_3 , Ta_2O_5 and Nb_2O_5 oxides were supplied by Alfa Aesar, and the $\text{K}_2\text{CO}_3 \cdot 1.5\text{H}_2\text{O}$ hydrated potassium carbonate by Fluka. Prior to the deposition, the target was polished on dry 320 and 1200 grit SiC papers and cleaned by pulsed air.

The substrates were $5 \times 5 \text{ mm}^2$ single crystalline R-plane sapphire ($\text{Al}_2\text{O}_3(\bar{1}102)$), Joint Committee on Powder Diffraction Standards (JCPDS) card 00-010-0173, SG: $R\bar{3}c$ ($N^\circ 167$), $a = 4.758 \text{ \AA}$, $c = 12.991 \text{ \AA}$) and $5 \times 5 \text{ mm}^2$ single crystal (001) SrTiO_3 (labelled STO; JCPDS card 01-073-0661, SG: $Pm\bar{3}m$ ($N^\circ 221$), $a = 3.905 \text{ \AA}$), both supplied by Crystal GmbH Company. They were ultrasonically cleaned in acetone during 5 min, then in isopropyl alcohol during 5 min, prior to the deposition step.

K-Ta-Nb-O (KTN) films were grown by PLD using a KrF excimer laser (Tuilaser Excistar, pulse duration of 20 ns, $\lambda = 248 \text{ nm}$) operating at 2 Hz with an energy of 210 mJ (corresponding to a fluence of 2 J.cm^{-2}). The target-substrate distance was fixed at 70

mm. During the deposition (30 min), the substrate temperature (845°C and 865°C) and the oxygen pressure (30 Pa) were kept constant. After deposition, samples were routinely cooled from deposition temperature down to room temperature within 30 min, under an oxygen pressure of 2.67×10^4 Pa. Scanning electron microscopy (SEM) was performed by using field emission gun Jeol JSM 6301F and Jeol JSM 7100 instruments working at 7 kV and at 5.0 kV, respectively. Chemical composition of the samples was characterized by energy dispersive X-ray spectroscopy (EDXS) by using a Jeol JSM 7100 instrument working at 10 kV equipped with an Oxford Aztec EDS system. The samples were coated with carbon prior to the analysis. X-ray diffraction (XRD) in θ - 2θ mode was carried out using a θ - 2θ instrument (Bruker AXS D8 Advance) working with a monochromatized Cu K α 1 radiation and equipped with a 1D detector (192 channels). Data were collected across a 2θ range of 5-80°, using a 0.002° step and acquisition time of 0.3 s/step. Φ -scans and rocking curves were carried out using a 4-circle texture diffractometer (Bruker AXS D8 Discover) operating with a Cu K α radiation equipped with a 1D detector (192 channels). Reciprocal space maps (RSM) of film grown on SrTiO₃ (respectively on sapphire) were recorded on the same instrument equipped with a double Ge channel cut

monochromator (respectively without monochromator); the maps were displayed thanks to the DxTools free software¹⁹.

3. RESULTS AND DISCUSSION

3.1. Microstructure and preferential orientation

Scanning electron micrographs of KTN-TTB films grown on (001)STO at 845°C and on R-plane sapphire at 845 and 865°C are displayed in figure 3. Films are constituted of crystallites with two morphologies: i) elongated horizontal parallelepiped-shaped crystallites, distributed in two groups of variants growing at 90° from each other, and ii) vertical parallelepiped-shaped nanorods. On STO, large areas of the substrate are mainly covered by horizontal crystallites, that are about 1 µm long, 100 nm wide (fig. 3b) and 250 nm thick (fig. SI.1a). On the contrary, other areas are fully covered by vertical nanorods (fig. 3a), which are 50 to 100 nm wide, and 50 to 400 nm long (fig. 3b). For the film synthesized at 845°C on sapphire, the vertical rods have grown on the whole substrate (fig. 3c). Micrograph performed at a higher magnification on an edge of the samples shows also the presence of a layer made of horizontal elongated crystallites (fig. 3d). Film

deposited at 865°C on sapphire presents also two kinds of areas, either covered by vertical rods or only by layer made of horizontal crystallites. On sapphire, vertical rods are of 50 to 100 nm wide and 1 µm long (fig. 3d and fig. SI.1b). On both substrates, the vertical crystallites have grown between two adjacent horizontal crystallites.

The average compositions have been determined by EDXS on horizontal layer area and on vertical rods area (table 1). These measurements show that on a same substrate, the vertical and horizontal nanorods have similar values of measured composition. Samples grown on sapphire have the same measured composition, around K: 32 %, Nb: 23 %, Ta: 44 % (± 3 %) corresponding to a composition ratio around $K_5(Ta_{0.65}Nb_{0.35})_{10}O_x$, corresponding therefore to a partially filled TTB where 5 of the 6 A1 and A2 sites are occupied while measured composition of sample grown on STO indicates a higher amount of potassium and a slightly different metal ratio Ta/Nb, *i.e.* K: 38 %, Nb: 26 %, Ta: 35 % (± 3 %) corresponding to a composition ratio around $K_6(Ta_{0.6}Nb_{0.4})_{10}O_x$ and therefore to a filled TTB. The difference of composition can arise from to a difference in temperature leading at the substrate surface possibly to volatility of potassium and film/substrate diffusion effects as it has been previously observed for other systems^{20,21}.

Table 1. Average composition of KTN-TTB films analyzed by EDXS.

Samples	Vertical rods area		Horizontal rods area	
	Measured composition	Composition ratio	Measured composition	Composition ratio
KTN-(001)STO_845°C	K: 38.2 ± 3 % Nb: 26.8 ± 3 % Ta: 35 ± 3 %	$K_{6.2}(Ta_{0.57}Nb_{0.43})_{10}$	K: 37.5 ± 3 % Nb: 25.6 ± 3 % Ta: 36.9 ± 3 %	$K_6(Ta_{0.59}Nb_{0.41})_{10}$
KTN-R-sapphire_845°C	K: 32.2 ± 3 % Nb: 23.5 ± 3 % Ta: 44.3 ± 3 %	$K_{4.8}(Ta_{0.65}Nb_{0.35})_{10}$	K: 33.6 ± 3 % Nb: 22.5 ± 3 % Ta: 43.9 ± 3 %	$K_5(Ta_{0.66}Nb_{0.34})_{10}$
KTN-R-sapphire_865°C	K: 30.9 ± 3 % Nb: 23.5 ± 3 % Ta: 45.6 ± 3 %	$K_{4.5}(Ta_{0.66}Nb_{0.34})_{10}$	K: 31.6 ± 3 % Nb: 22.4 ± 3 % Ta: 46 ± 3 %	$K_{4.3}(Ta_{0.66}Nb_{0.34})_{10}$

Figure 4 shows the $\theta/2\theta$ XRD patterns of the KTN/(001)STO and KTN/sapphire films deposited at 845°C. Pattern of the sample deposited on sapphire at 865°C is similar to

that grown at 845°C (not shown). As seen in the figure 4a, in addition to substrates reflections, only 001 and 310 TTB reflections are present for both films indicating that the TTB film was preferentially oriented along one or the other (or both) of these directions. Indeed, the lattice spacings d_{001} and d_{310} for a TTB structure are almost equal (for KTN-TTB phase, $d_{001}^{TTB} = 3.975 \text{ \AA}$ and $d_{310}^{TTB} = a_{TTB}/\sqrt{10} = 3.964 \text{ \AA}$).

Magnification of the XRD pattern around the 002 and 620 reflections shows that for the KTN/(001)STO film this peak splits actually into two contributions with lattice spacings $d = 1.992 \pm 0.005 \text{ \AA}$ and $1.987 \pm 0.005 \text{ \AA}$ (fig. 4b). This splitting indicates that there are in fact two out-of-plane orientations in the film, namely [001] and $\langle 310 \rangle$. No splitting is observed for the KTN/sapphire film deposited at 845°C neither for the one grown at 865°C. This indicates that the lattice constants of the TTB are different on STO than on sapphire. This can be due either to a different strain state of the film as a function of the substrate or to the observed difference in composition (table 1). Indexation of these peaks gives the following lattice constants: $a_{TTB} = 12.570 \pm 0.005 \text{ \AA}$; $c_{TTB} = 3.984 \pm 0.005 \text{ \AA}$ on STO and $c_{TTB} = 3.975 \text{ \AA}$ on R-plane sapphire (table 2).

Table 2. Lattice constants of KTN-TTB phase determined by XRD in $\theta/2\theta$ mode and in asymmetric mode. The error value is ± 0.005 Å.

Types of nanorods	Measurement	Lattice constants on STO	Lattice constants on sapphire
Vertical nanorods	Asymmetric	$a_{\text{TTB}}^{\text{Ver}} = 12.550$ Å	$a_{\text{TTB}}^{\text{Ver}} = 12.570$ Å
	Symmetric	$c_{\text{TTB}}^{\text{Ver}} = 3.984$ Å	$c_{\text{TTB}}^{\text{Ver}} = 3.975$ Å
Horizontal nanorods	Symmetric	$a_{\text{TTB}}^{\text{Hor}} = 12.572$ Å	$a_{\text{TTB}}^{\text{Hor}} = 12.567$ Å
	Symmetric	$c_{\text{TTB}}^{\text{Hor}} = 3.967$ Å	$c_{\text{TTB}}^{\text{Hor}} = 3.970$ Å

Rocking-curves of the 001 and 310 TTb reflections on both substrates are shown in figure SI.2a. The peak of the film grown on sapphire is wider (full width at half maximum $\Delta\omega \sim 3^\circ$) than the one of the film grown on STO ($\Delta\omega = 0.9^\circ$), indicating for the former a more important mosaicity, created by slight misorientations of different grown crystallites.

3.2. Epitaxy study

From previous transmission electron microscopy experiments, the growth direction of vertical nanorods was determined as being $[001]^{17}$ (see scheme of this orientation in figure 2a, left). Consequently, the crystallites grown with the out-of-plane $\langle 310 \rangle$ preferential orientation correspond to the in-plane elongated crystallites, as schematized in figure 2a (center and right). To validate this assumption, phi-scans on vertical nanorods were performed on $\{311\}$ planes of the TTB phase, by orienting the sample at $2\theta = 31.72^\circ$ and $\chi \sim 45^\circ$ (calculated 45.11°), the latter angle corresponding to the angle between the (001) and $\{311\}$ planes. For the horizontal rods, phi-scans were performed on $\{210\}$ planes of TTB phase, by orienting the sample at $2\theta = 15.7^\circ$ and $\chi = 45^\circ$, the angle between $\{310\}$ and $\{210\}$ planes being equal to 45° . Figure 5 shows the results on both substrates. For both substrates, intensities from horizontal nanorods ($\{210\}$ phi-scan) are weaker than for vertical nanorods ($\{311\}$ phi-scan). This difference in intensity is likely related to a difference of relative intensity between 311 ($I = 999$) and 210 ($I = 379$) reflections, according to the JCPDS card n°01-087-1856 for the $K_6\text{Nb}_{10.88}\text{O}_{30}$ compound. In addition, SEM micrographs in Fig. 3 suggest a higher number of vertical nanorods compared to horizontal nanorods than can partially explain the differences in intensities for phi-scans.

3.2.1. Epitaxy of (001)-oriented vertical nanorods

On both substrates, phi-scans performed on {311} planes shows 12 peaks, *i.e.* 4 peaks of the same intensity and located at 90° from each other and 8 smaller peaks. The four most intense peaks are located at the same values of phi (ϕ) that the {110}STO peaks, and at $\pm 45^\circ$ and $\pm 135^\circ$ of the (0006) sapphire peak. Each smaller peak is located at about $\pm 37^\circ$ from a larger peak position. On sapphire, the smaller peaks have an intensity half that of the largest peaks (Fig. 5a). On STO, it is not possible to determine the relative intensities of both kinds of peaks due to substrate contribution to the peaks located at about 0, ± 90 and $\pm 180^\circ$ (Fig. 5b). Indeed, the reflection parameters for {110}STO planes are very close to that of the {311}TTB planes, *i.e.* $2\theta = 32.42^\circ$ and $\chi = 45^\circ$. Traces of {311} planes in the (001) plane of the TTB phase are parallel to the $\langle 310 \rangle$ directions. Therefore, the orientation relationships between the $\langle 100 \rangle$ direction of the substrate (cubic $\langle 100 \rangle$ for (001)STO, and pseudo-cubic $\langle 100 \rangle$ for sapphire) and the $\langle 310 \rangle$ directions of the TTB phase were determined from the phi-scans.

Figure 6a shows one of the possible in-plane orientations, labelled 1A in the figure. The tetragonal TTB unit cell is drawn in black lines and its in-plane ($[100];[010]$) orientation is defined by the black arrows. This unit cell is in-plane rotated of 18.43° relatively to that of the substrate drawn in the middle of the figure 6. $[1\bar{3}0]$ and $[310]$ directions of the TTB cell are then parallel to the $[100]$ and $[010]$ STO directions, respectively. With this particular orientation, it appears that the central square sub-unit defined by the potassium ions (red dashed lines) is parallel to the STO cell edges. By applying a mirror to this orientation perpendicularly to the $[1\bar{3}0]$ direction, the orientation 1B is obtained (fig. 6b), which is equivalent and equiprobable to the previous one: the central square pattern is still parallel to the substrate cell. Thus, 1A and 1B orientations are at the origin of peaks in the phi-scans located at the same values of ϕ (Fig. 5a, 5b). The out-of-plane orientation of the variant 1A is $[001]$, while that of the variant 1B is $[00\bar{1}]$. Orientations 1A and 1B are anti-phase domains. By applying to the crystal 1A, an in-plane clockwise rotation of $\phi = 53.13^\circ$, the orientation displayed in figure 6c is obtained, which corresponds in the phi-scan to a peak located at $\Delta\phi = + 53.13^\circ$ from the variant 1A peak. With this orientation, the $[3\bar{1}0]$ and $[130]$ directions are then parallel to the $[100]$ and $[010]$ STO directions, and

in this case, the square pattern located at the vertices of the cell (green dashed lines) is now parallel to the edges of the substrate cell. This orientation is also equiprobable to the orientations 1A and 1B.

Actually, this orientation is identical to 1B. By shifting the unit cell origin of $1/2\mathbf{a} + 1/2\mathbf{b}$ (shift of the black unit cell to the yellow cell in figure 6c), the cell drawn in figure 6b is recovered. By applying to these orientation a mirror perpendicular to the $[\bar{3}10]$ direction, another anti-phase domain is obtained (figure 6d), identical of the orientation 1A. This last orientation can also be obtained by rotating the crystal 1B by $\phi = 36.87^\circ$ clockwise and corresponds in the phi-scan to a peak located at $\Delta\phi = + 36.87^\circ$ from the variant 1B peak.

Figure 7 shows the corresponding positions in the phi-scans of supplementary rotations of $\phi = 36.87^\circ$ and 53.13° applied on the variants 1A and 1B. The most intense peak correspond to the presence of both orientations at the same phi-value, every 90° . Rotation of 1A by 53.13° leads to 1B alone while rotation of 1B by 36.87° leads to 1A alone. Therefore the intensity of the peaks located at these values (relatively to the strongest

peaks) are half that of the strongest peak. This conclusion is validated by simulating the {311} pole figures for each orientation.

Figure 8 presents the simulated pole figure of orientation 1A, superposed to that of domain 1B (*i.e.* superposition of domains oriented along [001]); twelve poles are then observed: four at $\phi = 90^\circ$ from each other, and for which the intensity is twice that of the eight other peaks located at $\phi = +36.87^\circ$ and $\phi = +57.13^\circ$ relatively to the four former peaks. This result agrees with the experimental pole figure displayed in figure 8b. Figure 2b is a schematic representation of these two variants, corresponding to vertical nanorods oriented on the STO substrate (left panel of the figure). Figure 6e is the superposition of the variant 1A with the STO lattice showing the coincidence between the unit cell constant a_{TTB} of the TTB cell and the diagonal of 3 x 1 unit cells of the substrate. Coincidence between the 2 lattices corresponds to $a_{\text{TTB}}^2 \approx a_{\text{STO}}^2 + (3a_{\text{STO}})^2$, which leads to $a_{\text{TTB}} = \sqrt{10} a_{\text{STO}}$. The in-plane rotation between the two cells is then equal to $\arctan(a_{\text{STO}}/3a_{\text{STO}}) = \arctan(1/3) = 18.43^\circ$. Therefore, each anti-phase domain corresponds to a disorientation of the TTB cell of $\pm 18.4^\circ$ relatively to the substrate cell.

The epitaxy is due to the small lateral mismatch value determined by the following

relation: $((a_{\text{STO}} - d_{310}^{\text{TTB}}) / a_{\text{STO}}) \times 100 = -1.5 \%$ (on sapphire, the lateral mismatch value is about -13.3 %, considering the pseudo-cubic lattice constant $a_{\text{sapphire}} = 3.5 \text{ \AA}$). The epitaxial relationships are:

$$(001)\text{TTB} // (001)\text{STO}$$

$$\langle 310 \rangle \text{TTB} // [010]\text{STO}$$

$$\langle \bar{1}30 \rangle \text{TTB} // [100]\text{STO}$$

Figure 6f is the picture of domain 1A in cross-sectional view (the two variants are equivalent), showing that the interface between the crystallites and the substrate is expected to be flat. The rocking curves of the $\{311\}$ orientations, were measured on both substrates (figure SI.3b). Film mosaicity is of $\Delta\omega \sim 3^\circ$ on sapphire and $\Delta\omega \sim 0.4^\circ$ on STO, respectively which indicates again a more important disorientation of the nanorods on sapphire with respect to their growth direction, than on STO.

3.2.2. Epitaxy of (310)-oriented nanorods

Phi-scans performed on $\{210\}$ planes of the TTB on both substrates are shown in figure 5. One can observe 90° -spaced four peaks of same intensity, at the same azimuths that the ones of $\{110\}$ STO, and at $\pm 45^\circ$ and $\pm 135^\circ$ of the (0006)sapphire peak, respectively. This result confirms that the in-plane elongated crystallites observed by SEM are out-of-plane oriented along the $\langle 310 \rangle$ directions. The peaks at 0 and 180° correspond to the variants labelled 2A and 2B in figure 2b, and the 2 other peaks are related to the variants (labelled 3A and 3B, fig. 2b) which is in-plane rotated by 90° relatively to the former one. Intersections of $\{210\}$ planes with the (001) plane of the TTB phase are parallel to the $\langle 310 \rangle$ directions. Therefore, the orientation relationships between the in-plane [001] direction of the TTB phase and the in-plane $\langle 001 \rangle$ cubic (or pseudo-cubic) directions of the substrate can be determined from the phi-scans. Figure 9 is the corresponding scheme of the interface in cross-sectional view between the horizontal nanorods and the substrate. Similar results are obtained by considering the pseudo-cubic cell of the sapphire (*cf.* figure SI.3), except that the TTB cell is slightly disoriented of about 4° due to the angle between $(\bar{1}102)$ and $(0\bar{1}\bar{1}\bar{2})$ planes of sapphire (94°). This result is fully in agreement with the high resolution transmission electron microscopy (HRTEM)

micrographs published by Jia *et al.*²² on a $\text{Ca}_{0.28}\text{Ba}_{0.72}\text{Nb}_2\text{O}_6$ (CBN) thin film grown on (001)STO by PLD. Figure 9 shows the two variants 2A (fig. 9a) and 3A (fig. 9b); both have the same out-of-plane growth direction, namely [130], but are in-plane rotated from each other by 90° , the growth direction being the rotation axis.

These two variants are equivalent and equiprobable. The $[00\bar{1}]$ and $[\bar{3}10]$ directions of variant 2A are parallel to the a and b substrate directions, and similarly, the $[310]$ and $[001]$ directions of variant 3A are parallel to the a and b substrate directions. By applying a vertical mirror perpendicular to each direction, two other equivalent variants, 2B and 3B, are obtained as schematized in figure 2b. These variants are also anti-phase domains. One can observe here also that the square patterns located at the cell vertices (drawn with dashed lines in figure 9a) are parallel to the cubic cell of the substrate. As shown in fig. 9a, the orientation of both cells relatively to each other and their respective complex crystalline structures lead to a rough interface based on a substrate surface made of half-cell steps and terraces, as pointed out in the work of Jia *et al.*²² Figure 10 presents these two same variants in plane-view, showing that the lattice constant c of the TTB phase is systematically parallel to one of the substrate lattice constants. Pole figures

for these orientations were computed (fig. 10c and d) and superposed (fig. 10e): the obtained figure presents four poles oriented at 90° from each other, in agreement with the {210} phi-scan in the figure 5. The epitaxial relationships are:

$$\{310\}_{\text{TTB}} // (001)_{\text{STO}}$$

$$[001]_{\text{TTB}} // \langle 100 \rangle_{\text{STO}}$$

$$\langle \bar{3}10 \rangle_{\text{TTB}} // \langle 010 \rangle_{\text{STO}}$$

In the elongation direction, the lateral mismatch is equal to $((a_{\text{STO}} - c_{\text{TTB}}) / a_{\text{STO}}) \times 100 = -1.79\%$; in the other in-plane direction the mismatch is equal to $((a_{\text{STO}} - d_{310}^{\text{TTB}}) / a_{\text{STO}}) \times 100 = -1.5\%$. Although the above determined mismatches are small, there is no obvious lattice coincidence between the TTB and substrate cells across the interface, as schematized in fig. 9a. For sapphire, these two values are about -13.6 and -13.3 %, respectively. The rocking curves of the 210 reflections were measured on both substrates (figure SI.3c). Film mosaicity is $\Delta\omega \sim 3.5^\circ$ on sapphire and $\Delta\omega \sim 0.6^\circ$ on STO, respectively, enlightening again that crystallites on sapphire present larger disorientation relatively to the substrate than on STO.

3.2.3. Lattice constants

Although the KTN-TTB phase grows with epitaxial relationships on both substrates, the important difference between the relative mismatch values indicates that the film on STO is expected to be more strained than the film on sapphire. In order to confirm this point, the out-of-plane and in-plane lattice constants of the two kinds of nanorods (*i.e.* horizontally and vertically grown) were measured on both substrates. In addition to the out-of-plane lattice constants determined by symmetric $\theta/2\theta$ experiments (figure 4, table 2), asymmetric $\theta/2\theta$ scans and RSMs were recorded to measure the in-plane lattice constants of the phase, and compared with schemes of the reciprocal space for each variant. Figure 11 shows the symmetric (002)STO (fig. 11a), and asymmetric ($\bar{1}03$)STO (fig. 11b) and ($\bar{1}33$)STO (fig. 11c) maps. In the (002)STO map, the (002)_{Ver} (variant 1A) and (620)_{Hor} (2A,3A) reflections of the TTB phase are observed in agreement with the $\theta/2\theta$ scan displayed in figure 4 and to the scheme of the reciprocal space shown in the right part of the figure (in addition, several asymmetric maps are schematized in the figure 11b in which the reflections that appear in the (002) map (figure 11a) are encircled in

1
2
3
4 blue). In the experimental $(\bar{1}03)$ STO map (left map in figure 11b), the reflections due to
5
6
7 the TTB phase are observed below that of the substrate. A second map focused on these
8
9
10 film reflections was recorded in a mode that allows better signal to noise ratio conditions
11
12
13 (right map in the figure). The reflections that appear in the $(\bar{1}03)$ map, namely $(3\bar{1}3)_{\text{Ver}}$
14
15
16 (variant 1A), $(680)_{\text{Hor}}$ (2A) and $(\bar{3}9\bar{1})_{\text{Hor}}$ (3A) are encircled in red in schemes of the
17
18
19 reciprocal space areas in figure 11b, and resulting superposition is displayed in the right
20
21
22 panel of this figure. This scheme shows that $(3\bar{1}3)_{\text{Ver}}$ and $(\bar{3}9\bar{1})_{\text{Hor}}$ reflections are
23
24
25 superposed while the $(680)_{\text{Hor}}$ reflection is located just below the two previous ones.
26
27
28 Therefore, it is not possible to distinguish unambiguously the reflections due to the vertical
29
30
31 1A and horizontal 3A crystals, consequently the measurement of the lattice constant of
32
33
34 vertical crystal is not possible. Therefore, a third map was recorded by considering the
35
36
37 orientation described in figure 6e, and obtained after an in-plane rotation ϕ of the sample
38
39
40 of 18.4° relatively to the angular position corresponding to the $(\bar{1}03)$ STO map. In this
41
42
43 case, the $(\bar{1}33)$ STO map is obtained and only the vertical crystallites are able to diffract.
44
45
46 Figure 11c shows this experimental $(\bar{1}33)$ STO map, where both expected reflections (film
47
48
49 and substrate) are observed, together with a second map focused on the film reflection,
50
51
52
53
54
55
56
57
58
59
60

indexed as being $(0\ \overline{1}03)$ TTB reflection, as depicted in the scheme of the reciprocal space displayed in fig. 11c. From this result, the corresponding in-plane lattice constant is equal to $a_{\text{TTB}}^{\text{Ver}} = 12.55\ \text{\AA}$.

Concerning the horizontal crystallites, the lattice constant $c_{\text{TTB}}^{\text{Hor}}$ is equal to $3.967\ \text{\AA}$ from an asymmetric (210) STO scan that shows both reflections $(621)_{\text{Hor}}$ and $(312)_{\text{Ver}}$ (figure SI.4). RSMs were also recorded on the film grown on sapphire, but with $\text{Cu K}\alpha_{1,2}$ beam (figure SI.5). Indeed, with the use of the monochromator, the film reflection intensity was too weak to be detected, due to the small thickness and/or the mosaicity impact. One can observe in the symmetric map of KTN/sapphire (figure SI.5a) that the $(002)_{\text{Ver}}$ film reflection is not vertically aligned with the substrate reflection. This misorientation (about 4°) is due to the pseudo-cubic cell of sapphire that forms an angle of 94° instead of 90° and induces an inclination of the above film cell (*cf.* scheme in figure SI.3).

All the determined lattice constants on both substrates are listed in table 2. On sapphire, the lattice constants a_{TTB} and c_{TTB} are approximately the same for both horizontal and vertical nanorods. On STO on the contrary, the c_{TTB} lattice constant is slightly lower for the horizontal rods, than for the vertical rods, and accordingly the a_{TTB} is higher for the

horizontal rods than for the vertical rods indicating an in-plane compressive state of both kinds of rods. These results are in agreement with the small mismatch values determined for film grown on STO, while the films grown on sapphire are fully relaxed in reason of the large mismatch values. This also explains the greater crystallites disorientation on sapphire leading to the broadening of the rocking-curve.

3.3. Horizontal *versus* vertical nanorods

Since the determined lattice constants are rather similar for both kind of crystallites (vertical *vs* horizontal rods) whatever the substrate is, and since both kind of crystallites are growing on both substrates, it appears that the epitaxial mismatch is not at the origin of the growth of one kind of rods rather the second one. Infortuna *et al.* have demonstrated the influence of the last atomic plane of the STO substrate on the growth of $\text{Sr}_x\text{Ba}_{1-x}\text{Nb}_2\text{O}_6$ (SBN) TTB phase²³: if the substrate is terminated by a SrO plane, growth of a (001)-oriented columnar film is observed, while for TiO_2 -terminated plane, {310}-oriented rods are observed. Inversely, Jia *et al.*²² have shown that the growth of (001)-oriented domain of CBN, TTB is preferential on TiO_2 -termination in reason of a better atomic matching in

1
2
3 this configuration than on SrO-plane. Although these results look antagonist at the first
4
5
6
7 sight, they deal with two different compounds, that were moreover deposited at very
8
9
10 different partial oxygen pressures (between 200-400 mTorr for the former and at 1.5
11
12
13 mTorr for the latter) and at different deposition temperatures (between 730-760°C for the
14
15
16 former and between 600 and 800°C for the latter). Indeed, Ebina *et al.* have shown that
17
18
19 for SBN ($x = 0.5$) films grown on (La,Sr)TiO₃ substrate, the preferential orientations
20
21
22 depend both on the oxygen partial pressure and on the deposition temperature²⁴. We
23
24
25 have made preliminary experiments showing that the surface termination of the STO
26
27
28 substrate is a key parameter for the growth of KTN TTB nanorods either vertically or
29
30
31 horizontally. TiO₂-terminated surface involves the growth of horizontal rods only (these
32
33
34 results are not shown here, and will be the subject of another article). The TTB phases
35
36
37 often show an anisotropic growth with the *c* axis being the elongation direction. This
38
39
40 particular growth has been observed for materials obtained as powder, anisotropy of
41
42
43 particles being reinforced by different synthesis processes^{12,25-27}. Concerning thin films
44
45
46 of TTB phases, growth of epitaxial layer according a Volmer-Weber mode was reported
47
48
49 by only 3 groups, with either growth of horizontal rods by sol-gel method^{28,29}, and by PLD
50
51
52
53
54
55
56
57
58
59
60

after chemical treatment of the surface²³, or columnar growth by PLD^{23,30}. As far we known, our study is the only one dealing with vertical nanorods perfectly isolated from each other.

3.4. Anti-phase domains

Previous studies on (001)SBN and CBN TTB thin films grown on (001)STO, (001)LaNiO₃/CeO₂/YSZ/Si and (001)MgO substrates have shown that films form in-plane antiphase domains as observed in the present study^{20,21,28–35}. On MgO in particular, 3 kinds of domains have been determined, whatever the synthesis method is, with 0°, ± 18.43° (= arctan(1/3)), et ± 30.96° (= arctan(3/5)) in-plane orientations (sometimes simultaneously) relatively to the main directions of the substrate. Growth on MgO of domains turned by ± 18.43° is considered as a minimal electrostatic energy configuration³¹. Willmott *et al.* have shown that the proportion of each domain (0°, ± 18.43°, ± 30.96°) in a same film of SBN was a function of the amount x, with a predominance (~ 90 %) for domains at ± 18.43° for x ≥ 0.55³⁶, although this is the configuration for which the mismatch is the most important. On the contrary, on STO, only

the domains oriented at $\pm 18.43^\circ$ in the plane have been observed (with mismatch values of 0.83 % and 1.58 % for CBN)^{22,23}, in agreement with our results. No results on sapphire have been reported so far.

The factors that control the epitaxial growth are the misfit along the interface, the density of coincident atom sites at the interface and the nature of the chemical interaction at the interface^{38,39}. In case of usual (001)ABO₃ perovskite growth on (001)A'B'O₃ perovskite substrate (for instance, KNbO₃ on SrTiO₃ which is a system chemically close to the present one), the epitaxy is characterized by a cube-on-cube growth and an alignment of the perovskite subunits (PSU) of the substrate with those of the film at the interface. This results in the following sequence of layers at the interface: BO₂/AO/BO₂/A'O/B'O₂ or BO₂/AO/B'O₂/A'O (for instance TiO₂/SrO/TiO₂/KO/NbO₂ or TiO₂/SrO/NbO₂/KO).

Regarding the epitaxial growth of the KTN TTB phase on STO, three different epitaxy configurations can be examined: i) a cube-on-cube growth with the tetragonal TTB cell parallel to the STO cell, corresponding to the growth on one cell of TTB on nine cells of STO, ii) a TTB PSU growth on STO PSU, iii) a domain matching epitaxy (DME, see below). We have calculated the mismatch of these 3 configurations (*cf.* table 3).

Table 3. Mismatch values between TTB cell and STO cell for the three different epitaxy configurations.

Out-of-plane orientation	Cube-on-cube mismatch	TTB PSU on STO PSU mismatch	DME mismatch
(001)	-7.01 %	-0.38 %	-1.52 %
(130)	-7.01 %	-0.38 %	-1.52 %
	-1.79 %	-1.79 %	-1.79 %

If the lattices were superposed cube-on-cube (*i.e.* one cell of TTB on nine cells of STO), the mismatch will be equal to $\Delta a/a = (3a_{\text{STO}} - a_{\text{TTB}})/3a_{\text{STO}} = -7\%$ (12.2 and -19.4 % in the case of sapphire). In the case of SBN grown on (001)MgO, the mismatch would be equal to -1.1 % if the film follows such configuration whereas it is equal to -6.2 % for the experimental growth actually observed with in-plane domains at $\pm 18.43^\circ$ ³². Therefore, it may be surprising to observe such growth if only the lattice coincidence is considered, but cube-on-cube growth will actually result in a charges conflict at several lattice

positions. Jia *et al.* have simulated the cube-on-cube configuration for CBN TTB on STO and shown that there were no coincidence between both lattices²².

It could be expected that the perovskite sub-units of the TTB cell are aligned on the perovskite cell substrate (which is actually not what it is observed here). The TTB PSU have for dimensions 3.92 Å in the (*a*, *b*) plane and 3.975 Å along *c*, which would correspond to mismatch values of $\Delta a/a = (a_{\text{STO}} - a_{\text{TTB-PSU}})/a_{\text{STO}} = -0.38\%$ for the vertical nanorods, and -0.38 % and -1.79 % for the horizontal nanorods if a TTB PSU was grown on a STO PSU. These mismatch values are very small. We have simulated this configuration, *i.e.* (001) TTB PSU on (001)STO PSU for cations and oxygen ions of both structures (fig. 12a and 12b). It is observed that this configuration presents actually a poor degree of coincidence between cations and anions of both structures. As seen above, the experimental results have shown that the actual configuration for the (001) texture, is the coincidence of the lattice constant a_{TTB} of the TTB cell with the diagonal of 3 x 1 unit cells of the substrate (Figure 6e), indicating that the growth is governed by other phenomena. The complex epitaxy observed here can be described in the framework of the domain matching epitaxy (DME), in which the epitaxial growth is governed by domain orientation

relationships where m lattice units of the film match with p lattice units of the substrate, with in our case an in-plane rotation of the epilayer relative to that of the substrate^{39,40}. Zheleva *et al.* have shown that the DME takes place because this configuration is energetically favourable compared to the lattice epitaxial growth³⁸.

Jia *et al.* have shown that the epitaxy of CBN on STO in the form of domains oriented at 18.43° corresponds to a high degree of coincidence between the cations of the TTB phase and that of the substrate, and that is the same for oxygen anions of the two structures²². In particular, there is a coincidence of the cations located on the A1 sites of the TTB phase with the Sr ions of STO, and a good match between the A2 cations with the Sr ions. Regarding the B1 and B2 cations, there is coincidence with the Ti cations of the substrate for 20 % of them, a good match for other 20 %, and no match for the remaining 40 %. Finally, for the $\langle 310 \rangle$ -oriented domains, the faceting allows the interface planes to avoid the areas of the structure where there is a bad lattice fit. Similarly to CBN on STO, we have simulated the growth of (001) (fig. 12c,d) and (310) (figure SI.6) KTN TTB phase in plane-view with respect of cations and anions positions relatively to those of the substrate. Actually, if we observe also a coincidence between A1 of (001) TTB with

the cations of (001)STO, the matching between the B1/B2 sites of TTB with the Ti cations of STO is less good for KTN than for CBN (fig. 12c), and the coincidence sites of oxygen ions (fig. 12d) are less numerous than for the cations lattices. Mismatches between CBN and STO are equal to - 0.83% and 1.58 %, whereas our results for KTN on STO leads to values of -1.52 % and -1.79 %. Concerning the (310) growth, the coincidence between elements of the film and those of the substrate in plane-view is clearly evidenced in the figure SI.6. In addition, if there is no obvious coincidence in cross-sectional view between film and substrate (fig. 9a), one can observe a lattice coincidence between the TTB phase and the substrate along the orange solid lines drawn in the figure 9a, corresponding to the $(210)_{\text{TTB}}$ planes, on which the cations of both structures are perfectly aligned, at least in the first cell layer of the film. These lines are aligned along the $\langle 011 \rangle$ STO direction, thus tilted by 45° relatively to the substrate surface. Therefore, we observed here, instead of the usual matching between the out-of-plane edges of the substrates cell and those of the epilayer, a 'tilted epitaxy' with the following matching $d_{001}^{\text{STO}} (=11.04 \text{ \AA}) \sim 2d_{210}^{\text{TTB}} (= 11.24 \text{ \AA})$.

5. CONCLUSION

In conclusion, we have reported the growth of epitaxial KTN tetragonal bronze films by pulsed laser deposition. Characterization by scanning electron microscopy showed films made of horizontal and vertical nanorods. X-ray diffraction analyses evidenced that the horizontal rods have a $\langle 310 \rangle$ out-of-plane preferential orientation while the vertical nanorods have a $[001]$ preferential orientation. In both cases, the nanorods exhibit complex epitaxy relationships with the two studied substrates, *i.e.* $(001)\text{SrTiO}_3$ and R-plane sapphire. For the $[001]$ growth, antiphase domains rotated in-plane by $\pm 18.43^\circ$ with respect to the $\langle 100 \rangle$ direction of the cubic (or pseudo-cubic for sapphire) of the substrate were observed. For the $[310]$ growth, antiphase domains are also observed, and they are also rotated out-of-plane by $\pm 18.43^\circ$ with respect to the out-of-plane direction of the substrates. The $[001]$ is then parallel to the substrate surface. The different possible configurations result in 6 variants on the same substrate. Among different models, this complex epitaxy is best described in the framework of the domain matching epitaxy, for which the degree of coincidence between cations (anions) of the film and those of the substrate is much higher than other possible epitaxy configurations. Since the polarization

direction of ferroelectric TTB phases are along the [001] direction, it is observed here the possibility to tailor this direction with the deposition temperature or the substrate surface preparation. Indeed, the ability of this phase to grow as vertical isolated nanorods opens interesting perspectives as potential materials for integrated piezoelectric nanogenerators or nanotransducers for stimulation in nanomedicine.

ASSOCIATED CONTENT

Supporting Information. The following files are available free of charge. Cross-sectional SEM; Rocking-curves; Scheme of interface between TTB and sapphire; Asymmetric XRD $2\theta/\omega$ scan (.pdf file).

AUTHOR INFORMATION

Corresponding Author

* valerie.demange@univ-rennes1.fr

Author Contributions

The manuscript was written through contributions of all authors. All authors have given approval to the final version of the manuscript.

Funding Sources

ISCR and ScanMAT received a financial support from the Région Bretagne, Rennes Métropole, the Département d'Ille et Vilaine and the European Union (CPER-FEDER 2007–2014, Présage Nos. 39126 and 37339, and CPER 2015-2020 MULTIMAT ScanMAT).

ACKNOWLEDGEMENTS

Scanning Electron Microscopy was performed on ScanMAT facilities platforms (UMS 2001, University of Rennes 1-CNRS). Dr André Perrin is warmly acknowledged for fruitful discussions.

ABBREVIATIONS

CBN, $\text{Ca}_{0.28}\text{Ba}_{0.72}\text{Nb}_2\text{O}_6$; DME, domain matching epitaxy; EDXS, energy dispersive X-ray spectroscopy; HRTEM, high resolution transmission electron microscopy; JCPDS, Joint Committee on Powder Diffraction Standards; KNN, $(\text{K},\text{Na})\text{NbO}_3$; KTN, $\text{K}_{5.06}(\text{Ta}_{0.57}\text{Nb}_{0.43})_{10.99}\text{O}_{30}$; PLD, pulsed laser deposition; PSU, perovskite subunits; PZT, $\text{PbZr}_{1-x}\text{Ti}_x\text{O}_3$; RSM, Reciprocal space maps; SBN, $\text{Sr}_x\text{Ba}_{1-x}\text{Nb}_2\text{O}_6$; SEM, Scanning electron microscopy; STO, SrTiO_3 ; TTB, Tetragonal tungsten bronze phases; XRD, X-ray diffraction.

REFERENCES

- (1) Bowen, C. R.; Kim, H. A.; Weaver, P. M.; Dunn, S. Piezoelectric and Ferroelectric Materials and Structures for Energy Harvesting Applications. *Energy Environ. Sci.* **2014**, *7*, 25–44. <https://doi.org/10.1039/c3ee42454e>.
- (2) European Parliament, Council of the European Union. EU-Directive 2002/95/EC. Restriction of the Use of Certain Hazardous Substances in Electrical and Electronic Equipment (RoHS). 2003, pp 19–23.
- (3) European Parliament, Council of the European Union. EU-Directive 2002/96/EC, “Waste Electrical and Electronic Equipment (WEEE). 2003, pp 24–38.

- (4) Jaffe, H. Piezoelectric Ceramics. *J. Am. Ceram. Soc.* **1958**, *41*, 494–498. <https://doi.org/10.1111/j.1151-2916.1958.tb12903.x>.
- (5) Li, J.-F.; Wang, K.; Zhu, F.-Y.; Cheng, L.-Q.; Yao, F.-Z. (K, Na)NbO₃-Based Lead-Free Piezoceramics: Fundamental Aspects, Processing Technologies, and Remaining Challenges. *J. Am. Ceram. Soc.* **2013**, *96*, 3677–3696. <https://doi.org/10.1111/jace.12715>.
- (6) Rödel, J.; Webber, K. G.; Dittmer, R.; Jo, W.; Kimura, M.; Damjanovic, D. Transferring Lead-Free Piezoelectric Ceramics into Application. *J. Eur. Ceram. Soc.* **2015**, *35*, 1659–1681. <https://doi.org/10.1016/j.jeurceramsoc.2014.12.013>.
- (7) Kumar, B.; Kim, S.-W. Recent Advances in Power Generation through Piezoelectric Nanogenerators. *J. Mater. Chem.* **2011**, *21*, 18946–18958. <https://doi.org/10.1039/c1jm13066h>.
- (8) Jung, J. H.; Lee, M.; Hong, J.-I.; Ding, Y.; Chen, C.-Y.; Chou, L.-J.; Wang, Z. L. Lead-Free NaNbO₃ Nanowires for a High Output Piezoelectric Nanogenerator. *ACS Nano* **2011**, *5*, 10041–10046. <https://doi.org/10.1021/nn2039033>.
- (9) Neurgaonkar, R. R.; Oliver, J. R.; Cory, W. K.; Cross, L. E.; Viehland, D. Piezoelectricity in Tungsten Bronze Crystals. *Ferroelectrics* **1994**, *160*, 265–276. <https://doi.org/10.1080/00150199408222463>.
- (10) Simon, A.; Ravez, J. Solid-State Chemistry and Non-Linear Properties of Tetragonal Tungsten Bronzes Materials. *C.R. Chim.* **2006**, *9*, 1268–1276. <https://doi.org/10.1016/j.crci.2006.04.001>.
- (11) Josse, M.; Bidault, O.; Roulland, F.; Castel, E.; Simon, A.; Michau, D.; Von der Muehl, R.; Nguyen, O.; Maglione, M. The Ba₂LnFeNb₄O₁₅ “Tetragonal Tungsten Bronze”: Towards RT Composite Multiferroics. *Solid State Sci.* **2009**, *11*, 1118–1123. <https://doi.org/10.1016/j.solidstatesciences.2009.02.015>.
- (12) Brik, F.; Enjalbert, R.; Roucau, C.; Galy, J. TTB Structure of K₄Ce₂M₁₀O₃₀ (M=Nb or Ta): Crystal Growth and Joint X-Ray and HREM Studies. *J. Solid State Chem.* **1996**, *122*, 7–14. <https://doi.org/10.1006/jssc.1996.0073>.
- (13) Miseki, Y.; Kudo, A. Water Splitting over New Niobate Photocatalysts with Tungsten-Bronze-Type Structure and Effect of Transition Metal-Doping. *Chemsuschem* **2011**, *4*, 245–251. <https://doi.org/10.1002/cssc.201000180>.
- (14) Yao, Y. B.; Mak, C. L.; Ploss, B. Phase Transitions and Electrical Characterizations of (K_{0.5}Na_{0.5})_{2x}(Sr_{0.6}Ba_{0.4})_{5-x}Nb₁₀O₃₀ (KNSBN) Ceramics with ‘unfilled’ and ‘filled’ Tetragonal Tungsten-Bronze (TTB) Crystal Structure. *J. Eur. Ceram. Soc.* **2012**, *32*, 4353–4361. <https://doi.org/10.1016/j.jeurceramsoc.2012.07.034>.
- (15) Lin, K.; You, L.; Li, Q.; Chen, J.; Deng, J.; Xing, X. Thermal Expansion Anomaly in TTB Ferroelectrics: The Interplay between Framework Structure and Electric Polarization. *Inorg. Chem.* **2016**, *55*, 8130–8139. <https://doi.org/10.1021/acs.inorgchem.6b01242>.
- (16) Zhu, X.; Fu, M.; Stennett, M. C.; Vilarinho, P. M.; Levin, I.; Randall, C. A.; Gardner, J.; Morrison, F. D.; Reaney, I. M. A Crystal-Chemical Framework for Relaxor versus Normal Ferroelectric Behavior in Tetragonal Tungsten Bronzes. *Chem. Mater.* **2015**, *27*, 3250–3261. <https://doi.org/10.1021/acs.chemmater.5b00072>.
- (17) Simon, Q.; Dorcet, V.; Boullay, P.; Demange, V.; Députier, S.; Bouquet, V.; Guilloix-Viry, M. Nanorods of Potassium Tantalum Niobate Tetragonal Tungsten Bronze Phase Grown by Pulsed Laser Deposition. *Chem. Mater.* **2013**, *25*, 2793–2802. <https://doi.org/10.1021/cm401018k>.
- (18) Rousseau, A.; Laur, V.; Deputier, S.; Bouquet, V.; Guilloix-Viry, M.; Tanne, G.; Laurent, P.; Huret, F.; Perrin, A. Influence of Substrate on the Pulsed Laser Deposition Growth and Microwave Behaviour of KTa_{0.6}Nb_{0.4}O₃ Potassium Tantalate Niobate Ferroelectric Thin Films. *Thin Solid Films* **2008**, *516*, 4882–4888. <https://doi.org/10.1016/j.tsf.2007.09.029>.
- (19) Boule, A. DxTools: Processing Large Data Files Recorded with the Bruker D8 Diffractometer. *J. Appl. Crystallogr.* **2017**, *50*, 967–974. <https://doi.org/10.1107/S1600576717005192>.

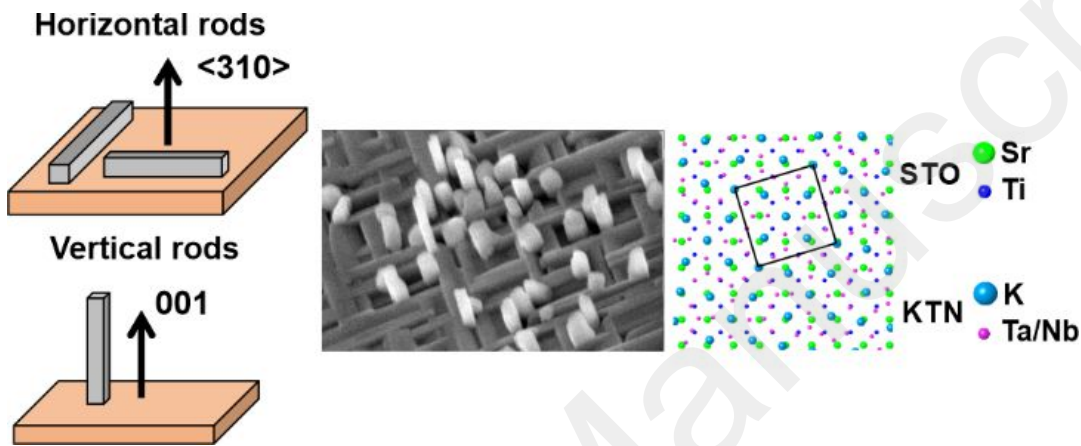
- (20) Willmott, P. Deposition of Complex Multielemental Thin Films. *Prog. Surf. Sci.* **2004**, *76*, 163–217. <https://doi.org/10.1016/j.progsurf.2004.06.001>.
- (21) Ma, C.; Chen, C. Pulsed Laser Deposition for Complex Oxide Thin Film and Nanostructure. In *Advanced Nano Deposition Methods*; John Wiley & Sons, Ltd, 2016; pp 1–31. <https://doi.org/10.1002/9783527696406.ch1>.
- (22) Jia, C. L.; Schubert, J.; Heeg, T.; Mi, S. B.; Chen, H. Y.; Joschko, B.; Burianek, M.; Muhlberg, M.; Urban, K. Tailoring the Orientations of Complex Niobate Films on Perovskite Substrates. *Acta Mater.* **2006**, *54*, 2383–2391. <https://doi.org/10.1016/j.actamat.2006.01.011>.
- (23) Infortuna, A.; Muralt, P.; Cantoni, M.; Setter, N. Epitaxial Growth of (SrBa)Nb₂O₆ Thin Films on SrTiO₃ Single Crystal Substrate. *J. Appl. Phys.* **2006**, *100*, 104110. <https://doi.org/10.1063/1.2372577>.
- (24) Ebina, Y.; Higuchi, T.; Hattori, T.; Tsukamoto, T. Ferroelectric and Structural Properties of Sr_{0.5}Ba_{0.5}Nb₂O₆ Thin Films on La_{0.05}Sr_{0.95}TiO₃ Substrate. *Jpn. J. Appl. Phys.* **2006**, *45*, 7300–7304. <https://doi.org/10.1143/JJAP.45.7300>.
- (25) Debnath, T.; Roy, S. C.; Ruescher, C. H.; Hussain, A. Synthesis and Characterization of Niobium-Doped Potassium Tetragonal Tungsten Bronzes, K_xNb_yW_{1-y}O₃. *J. Mater. Sci.* **2009**, *44*, 179–185. <https://doi.org/10.1007/s10853-008-3101-4>.
- (26) Madaro, F.; Saeterli, R.; Tolchard, J. R.; Einarsrud, M.-A.; Holmestad, R.; Grande, T. Molten Salt Synthesis of K₄Nb₆O₁₇, K₂Nb₄O₁₁ and KNb₃O₈ Crystals with Needle- or Plate-like Morphology. *CrystEngComm* **2011**, *13*, 1304–1313. <https://doi.org/10.1039/c0ce00413h>.
- (27) Lan, C.; Gong, J.; Wang, Z.; Yang, S. Synthesis of K₆Ta_{10.8}O₃₀ Nanowires by Molten Salt Technique. *Mater. Sci. Eng. B.* **2011**, *176*, 679–683. <https://doi.org/10.1016/j.mseb.2011.02.004>.
- (28) Nishio, K.; Seki, N.; Thongrueng, J.; Watanabe, Y.; Tsuchiya, T. Preparation and Properties of Highly Oriented Sr_{0.3}Ba_{0.7}Nb₂O₆ Thin Films by a Sol-Gel Process. *J. Sol-Gel Sci. Technol.* **1999**, *16*, 37–45. <https://doi.org/10.1023/A:1008709104118>.
- (29) Nishio, K.; Watanabe, Y.; Tsuchiya, T. Epitaxial Growth of Sr_xBa_{1-x}Nb₂O₆ Thin Films Prepared from Sol-Gel Process. *J. Sol-Gel Sci. Technol.* **2003**, *26*, 245–250. <https://doi.org/10.1023/A:1020707317411>.
- (30) Mi, S. B.; Ha, C. L.; Urban, K.; Heeg, T.; Schubert, J. Growth of Ca_xBa_{1-x}Nb₂O₆ Thin Films on MgO(100) by Pulsed Laser Deposition. *J. Cryst. Growth* **2006**, *291*, 243–248. <https://doi.org/10.1016/j.jcrysgro.2006.02.039>.
- (31) Schwyn Thöny, S.; Youden, K.; Harris, J.; Hesselink, L. Growth of Epitaxial Strontium Barium Niobate Thin-Films by Pulsed-Laser Deposition. *Appl. Phys. Lett.* **1994**, *65*, 2018–2020.
- (32) Tanaka, K.; Nakagawara, O.; Nakano, M.; Shimuta, T.; Tabata, H.; Kawai, T. Epitaxial Growth of (Sr,Ba)Nb₂O₆ Thin Films by Pulsed Laser Deposition. *Jpn. J. Appl. Phys.* **1998**, *37*, 6142–6145. <https://doi.org/10.1143/JJAP.37.6142>.
- (33) Aoyagi, R.; Takeda, H.; Okamura, S.; Nishida, T.; Shiosaki, T. Epitaxial Growth of Tungsten Bronze (Sr,Ba)Nb₂O₆ Thin Films by Chemical Solution Deposition. In *Proceedings of the 2001 12th IEEE international symposium on applications of ferroelectrics, vols I and II*; Streiffer, S. K., Gibbons, B. J., Tsurumi, T., Eds.; 2001; pp 905–908.
- (34) Chiu, T. W.; Wakiya, N.; Shinozaki, K.; Mizutani, N. Growth of Highly (001)-Textured Strontium Barium Niobate Thin Films on Epitaxial LaNiO₃/CeO₂/YSZ/Si(100). *Thin Solid Films* **2003**, *426*, 62–67. [https://doi.org/10.1016/S0040-6090\(02\)01304-4](https://doi.org/10.1016/S0040-6090(02)01304-4).
- (35) Cuniot-Ponsard, M.; Desvignes, J. M.; Ea-Kim, B.; Leroy, E. Radio Frequency Magnetron Sputtering Deposition of Hetero-Epitaxial Strontium Barium Niobate Thin Films (Sr_xBa_{1-x}Nb₂O₆). *J. Appl. Phys.* **2003**, *93*, 1718–1724. <https://doi.org/10.1063/1.1535749>.

- (36) Willmott, P. R.; Herger, R.; Patterson, B. D.; Windiks, R. Experimental and Theoretical Study of the Strong Dependence of the Microstructural Properties of $\text{Sr}_x\text{Ba}_{1-x}\text{Nb}_2\text{O}_6$ Thin Films as a Function of Their Composition. *Phys. Rev. B* **2005**, *71*, 144114. <https://doi.org/10.1103/PhysRevB.71.144114>.
- (37) Ndione, P. F.; Gaidi, M.; Durand, C.; Chaker, M.; Morandotti, R.; Rioux, G. Structural and Optical Properties of Epitaxial $\text{Ca}_x\text{Ba}_{1-x}\text{Nb}_2\text{O}_6$ Thin Films Grown on MgO by Pulsed Laser Deposition. *J. Appl. Phys.* **2008**, *103*, 033510. <https://doi.org/10.1063/1.2838176>.
- (38) Zheleva, T.; Jagannadham, K.; Narayan, J. Epitaxial-Growth in Large-Lattice-Mismatch Systems. *J. Appl. Phys.* **1994**, *75*, 860–871. <https://doi.org/10.1063/1.356440>.
- (39) Narayan, J.; Larson, B. C. Domain Epitaxy: A Unified Paradigm for Thin Film Growth. *J. Appl. Phys.* **2003**, *93*, 278–285. <https://doi.org/10.1063/1.1528301>.
- (40) Zhang, K. H. L.; Lazarov, V. K.; Galindo, P. L.; Oropeza, F. E.; Payne, D. J.; Lai, H. H.-C.; Egdell, R. G. Domain Matching Epitaxial Growth of In_2O_3 Thin Films on Alpha- Al_2O_3 (0001). *Cryst. Growth Des.* **2012**, *12*, 1000–1007. <https://doi.org/10.1021/cg201474h>.

For Table of Contents Use Only

Complex epitaxy of tetragonal tungsten bronze K-Ta-Nb-O nanorods

V. Demange^{1,2*}, Q. Simon³, F. Gouttefangeas², L. Joanny², M. Guilloux-Viry^{1,2}



Growth of horizontal and vertical tetragonal tungsten bronze K-Ta-Nb-O nanorods on SrTiO₃

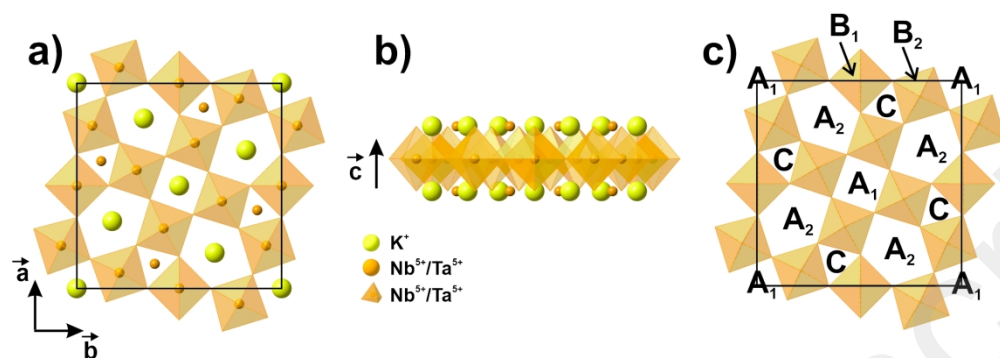


Figure 1. a) Projection of the KTN-TTB structure along the [001] direction. b) Projection of the TTB KTN structure along the [100] direction. c) Scheme of the TTB structure displaying the crystallographic sites.

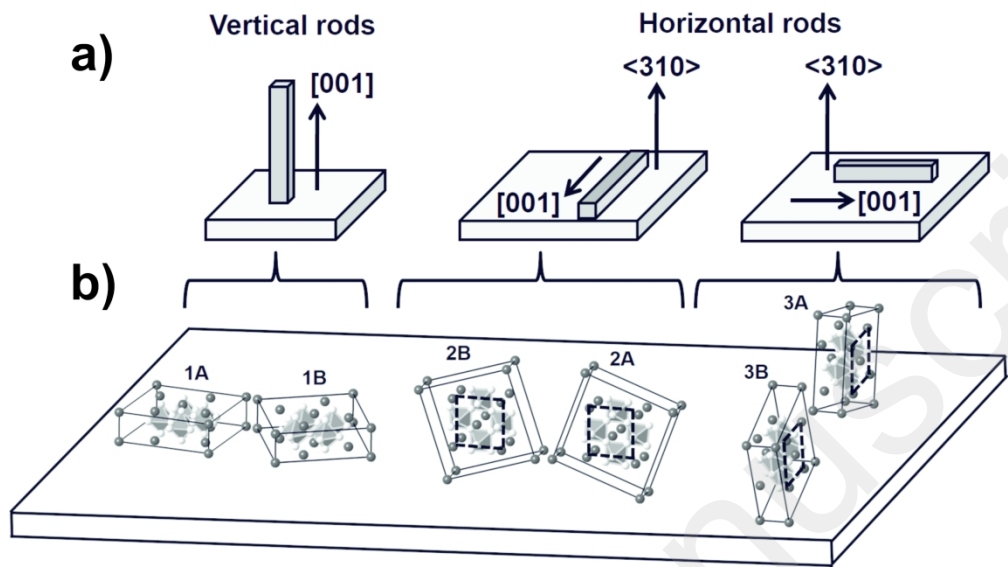


Figure 2. a) Scheme of the different orientations of the vertical and horizontal nanorods on the substrate. b) Scheme of all the possible orientations of the TTB phase on the substrate: on the left, vertical nanorods with two variants (labelled 1A and 1B), and on the right, horizontal nanorods with four variants (labelled 2 to 3).

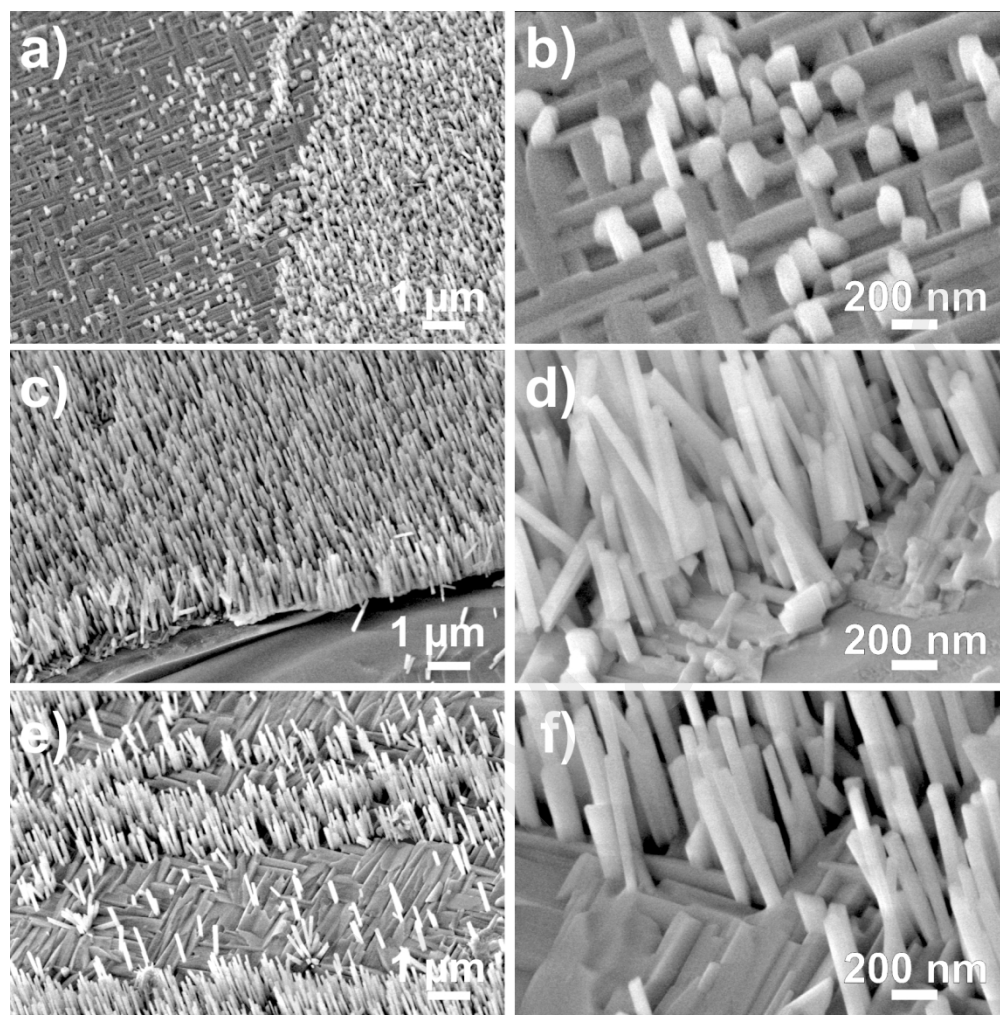


Figure 3. SEM micrographs at two different magnifications of KTN-TTB film deposited on (001)STO at 845°C (a,b), and of KTN-TTB films deposited on R-plane sapphire at 845°C (c,d) and at 865°C (e,f).

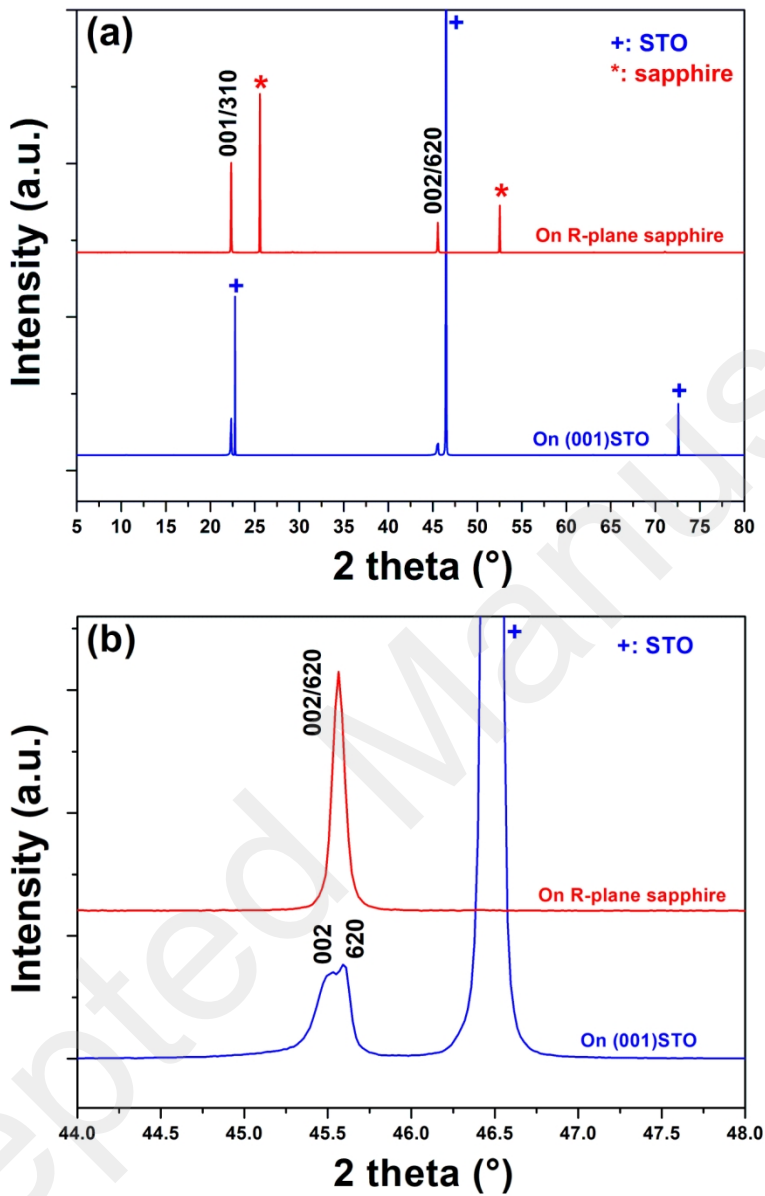


Figure 4. XRD patterns in $\theta/2\theta/2$ mode of the KTN-TTB films deposited on (001)STO (blue curves) and on R-plane sapphire (red curves): a) full-scale patterns; b) same patterns in $2\theta = 44\text{--}48^\circ$ range. The peaks are indexed according to the TTB structure (+: STO; *: sapphire).

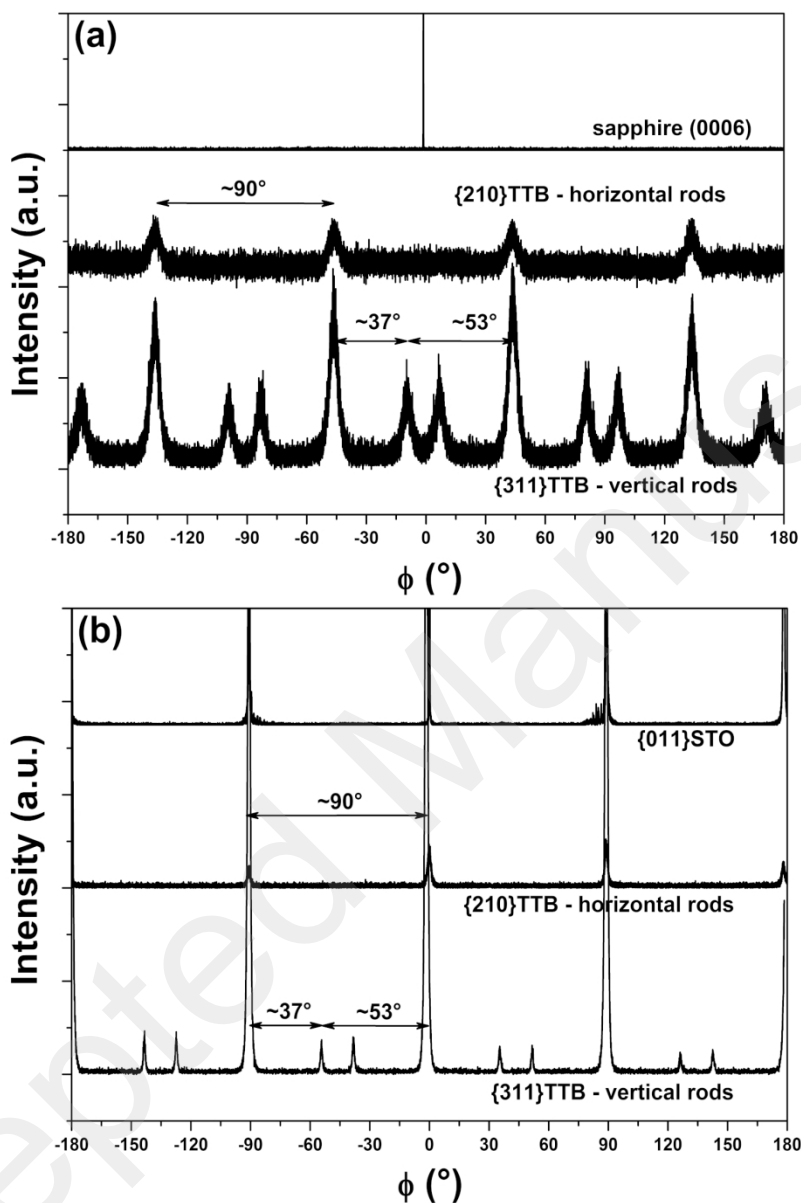


Figure 5. (a) ϕ -scans of KTN/sapphire film, carried out on (0006) sapphire plane, $\{210\}$ TTB planes of the horizontal nanorods, and $\{311\}$ TTB planes of the vertical nanorods. (b) ϕ -scans of KTN/STO film, carried out on $\{011\}$ STO planes, $\{210\}$ TTB planes of the horizontal nanorods, and $\{311\}$ TTB planes of the vertical nanorods.

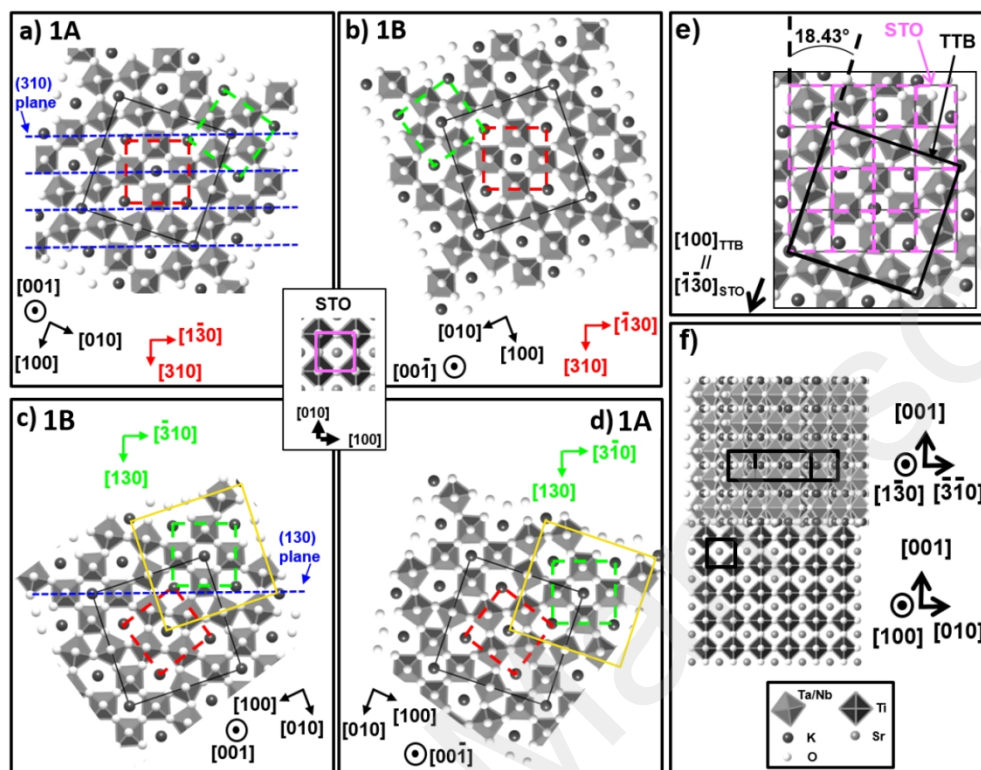


Figure 6. (a-d) Scheme of the two in-plane variants of the vertical nanorods on (001)STO, labelled 1A and 1B. The TTB cell is drawn with black solid lines. The orientations 1A (a) and 1B (b) correspond to two anti-phase domains related to each other by a vertical mirror plane. In these cases, the central sub-cell (red dashed lines) is parallel to the directions $[100]$ and $[010]$ of STO (STO cell is drawn in pink in the middle of the panel and in fig. 6e). c) Orientation 1A after an in plane rotation of $+53.13^\circ$. The shift of the unit cell (black cell to yellow cell) shows that this orientation is identical to the orientation 1B displayed in fig. 6b. d) Orientation 1B after an in plane rotation of $+36.87^\circ$. The shift of the unit cell (black cell to yellow cell) shows that this orientation is identical to the orientation 1A displayed in fig. 6a. (e) Superposition of the TTB phase on the STO lattice, showing the disorientation of 18.43° between the two cells. (f) Scheme of the domain 1A on STO in cross-sectional view.

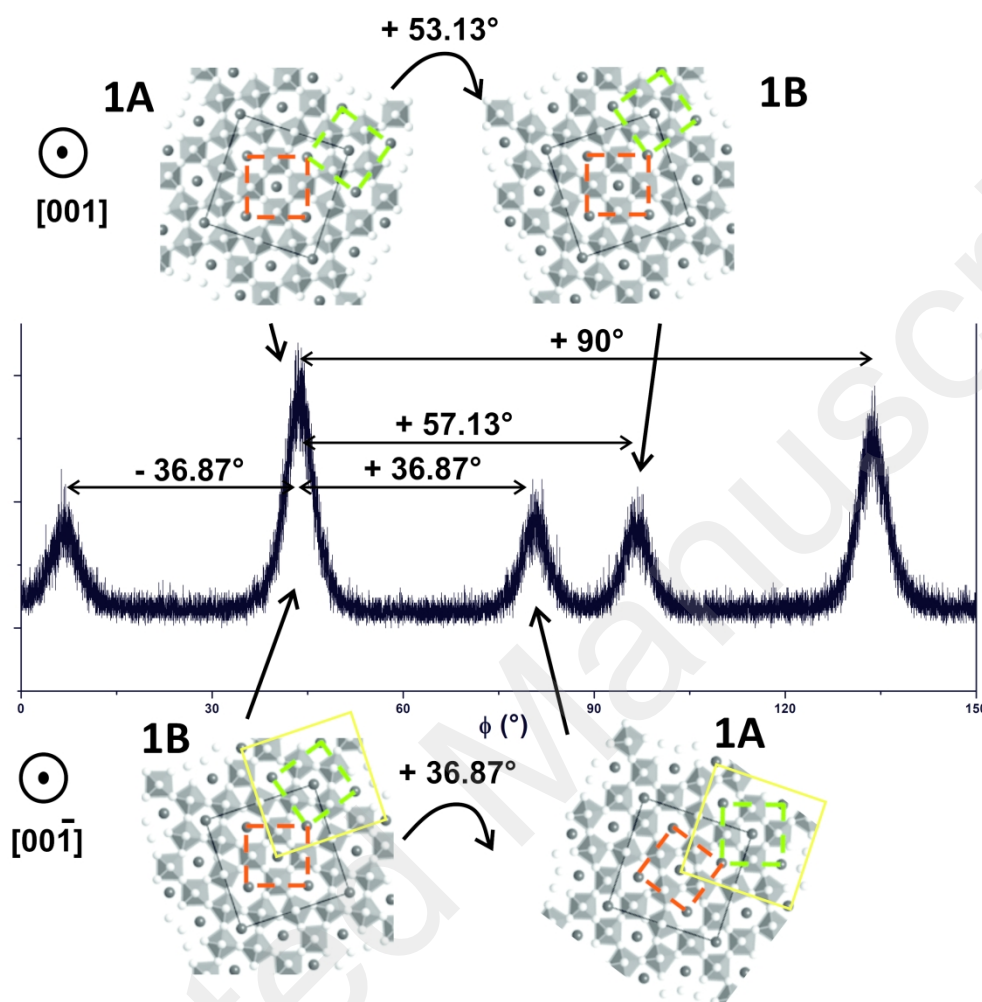


Figure 7. Occurrences of the different in-plane orientations of the vertical nanorods relative to the experimental corresponding ϕ -scan around $\{311\}$ TTB planes.

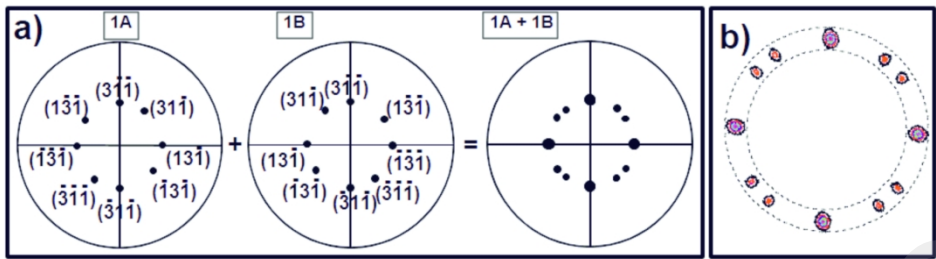


Figure 8. a) Modeling of $\{311\}$ pole figures of the TTB phase oriented along the domains 1A and 1B, and superposition of the pole figures two by two. b) Experimental pole figure of $\{311\}$ planes of the vertical nanorods.

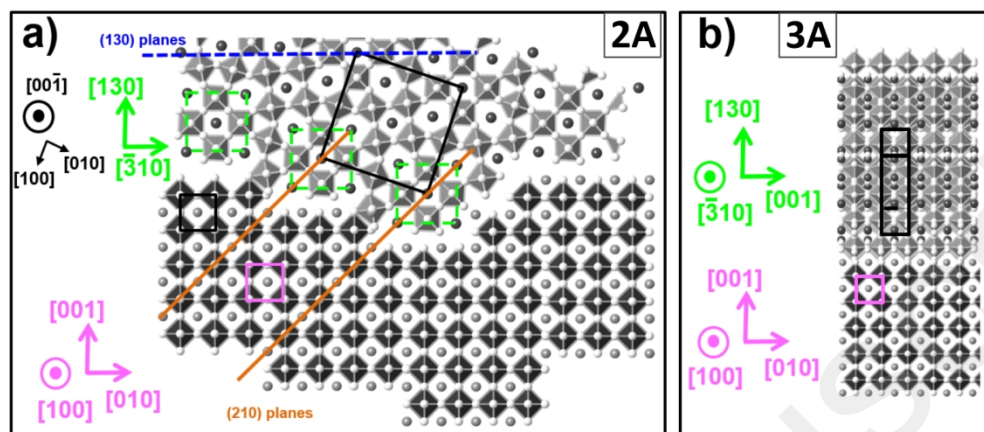


Figure 9. Modeling of the orientation of horizontal nanorods (light grey) on (001)STO (dark grey) in cross-sectional view: the variant 2A (a) is equivalent to the variant 3A (b) by rotation of 90° along the growth direction.

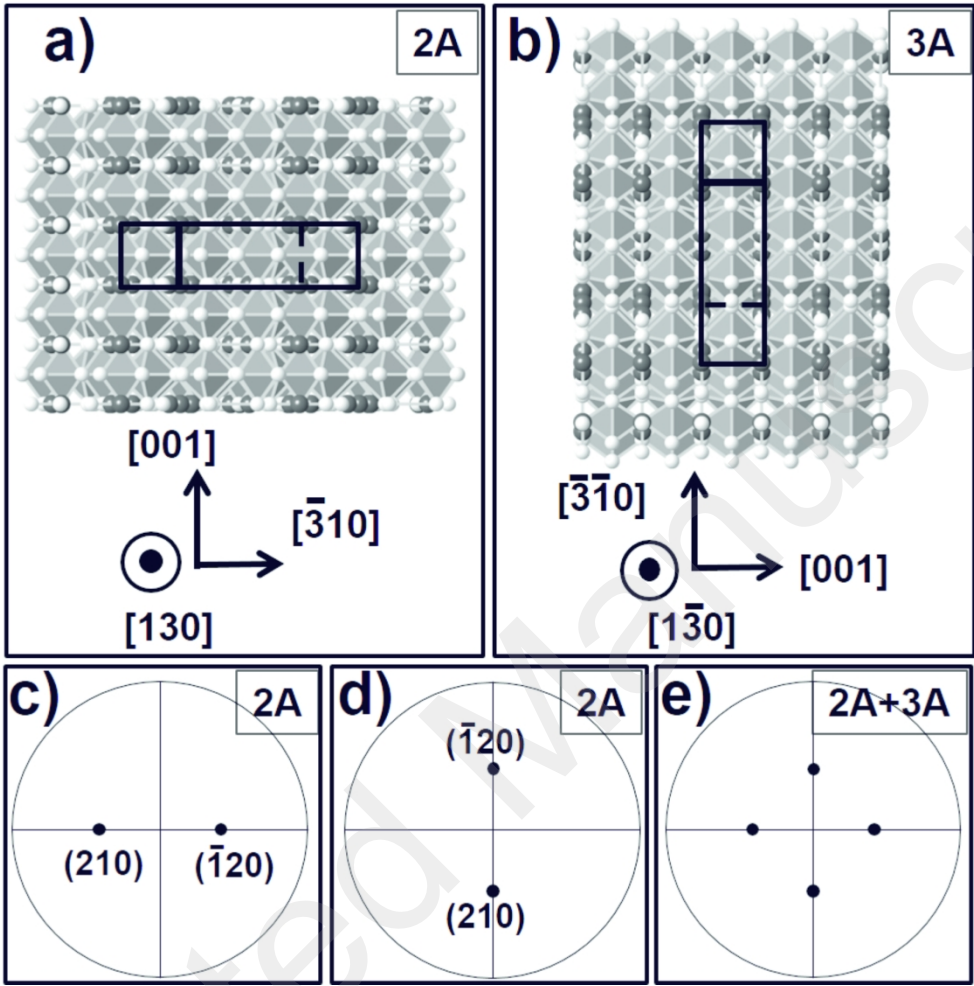


Figure 10. Modeling of the orientation of horizontal nanorods on (001)STO in plane-view (TTB cells are drawn with solid lines): the variant 2A (a) is equivalent to the variant 3A (b) by rotation of 90° along the growth direction. Modeling of the pole figures of the TTB phase oriented along the domains 2A (c) and 3A (d) and superposition of both pole figures (e).

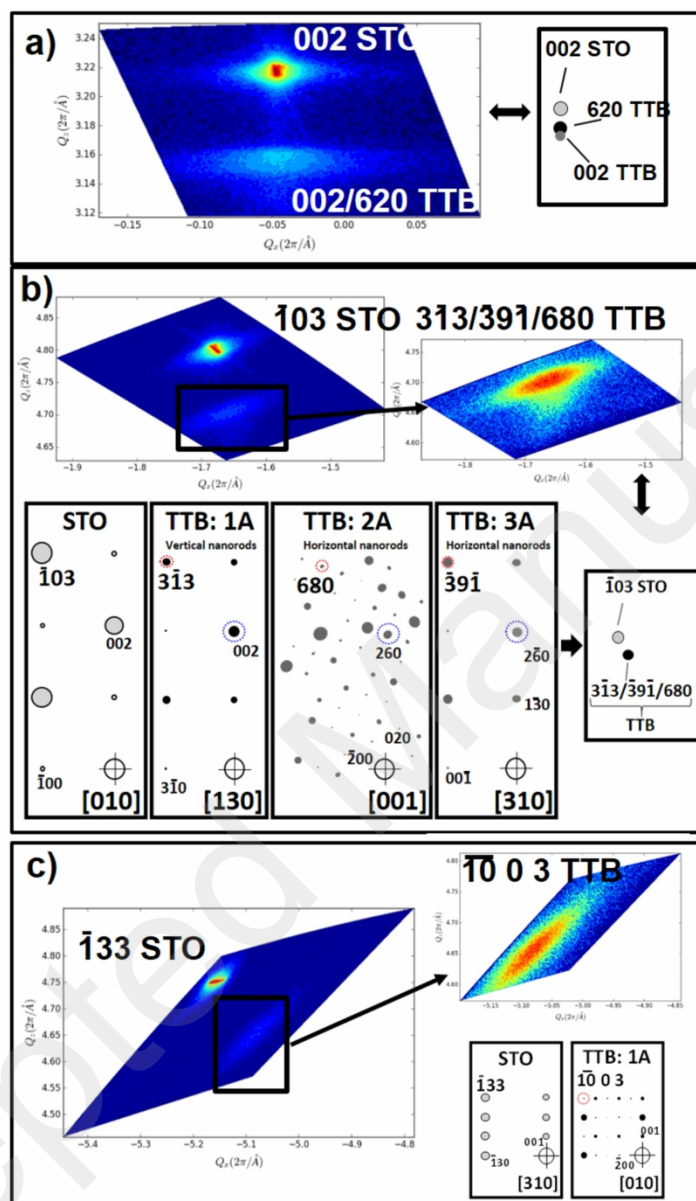


Figure 11. Reciprocal space maps of the KTN-TTB film on (001)STO: a) (002)STO RSM and corresponding scheme of the reciprocal space area. (b) (1 03)STO and (31 3)TTb RSMs and corresponding schemes of the reciprocal space areas. (c) (1 33)STO and ((10) 0 3)TTb RSMs and corresponding schemes of the reciprocal space areas.

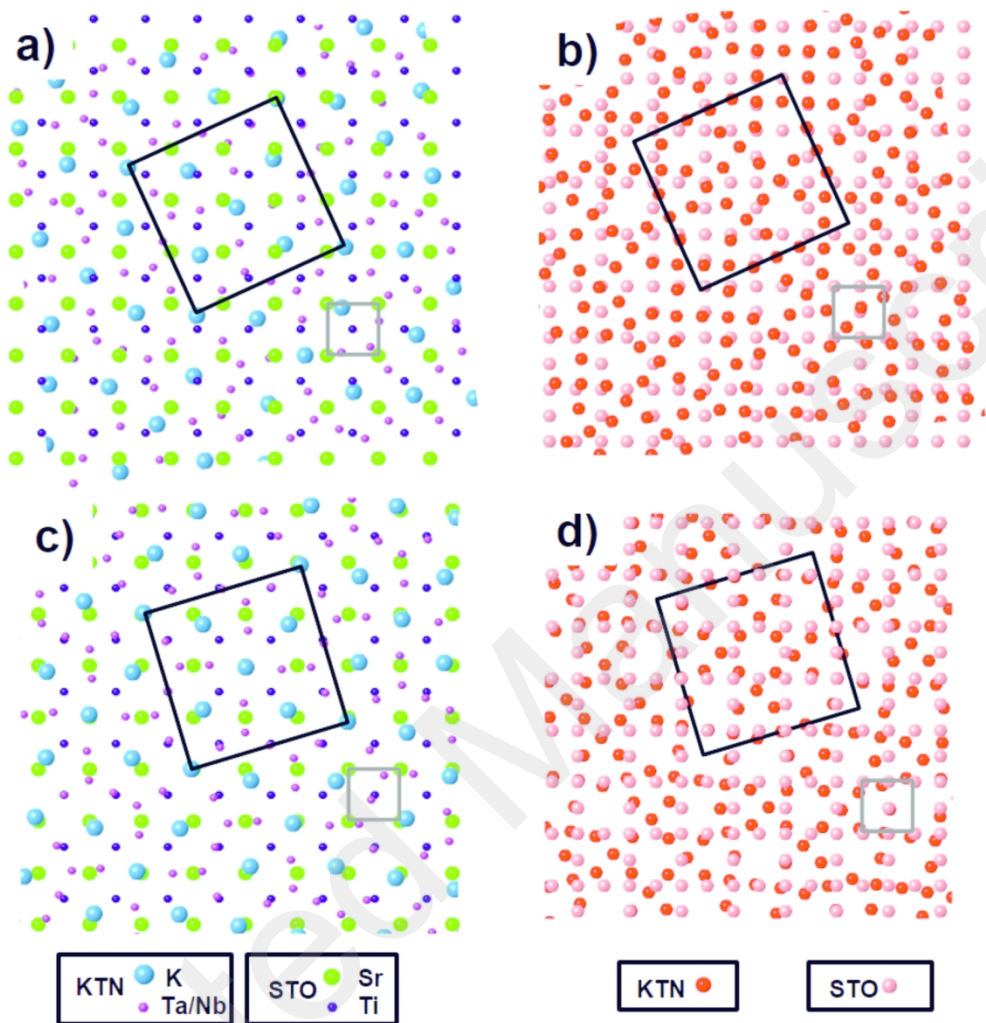


Figure 12. Superposition of the cationic (a) and anionic (b) lattices of the TTB and STO phases in the configuration in which (001) TTB perovskite sub-unit are aligned on (001) STO perovskite unit. Superposition of the cationic (c) and anionic (d) lattices of the TTB and STO phases with an in-plane disorientation of 18.43° between both cells (cells are drawn with solid lines: TTB (dark, STO (grey)).